Check for updates

study with material ID and respective compo- W5050 and W2200 are identical, except for the sintering ature (2200 °C for W2200 instead of 2400 °C for W5050 and all other materials).

Mat. ID	Number of samples	Composition
W5050	1	W
W2200	1	W
W2Y2O3	1	W + 2 wt% Y_2O_3
W1TiC	2	W + 1 wt% TiC
W2TiC	1	W + 2 wt% TiC
W3TiC	1	W + 3 wt% TiC
W0.5TaC	1	W + 0.5 wt% TaC
W1TaC	1	W + 1 wt% TaC

(see Table 1). The test procedure typically comprises tests at different THL power densities, number of pulses and base temperatures. Since the number of samples was so limited the testing conditions were fixed to a single parameter set: 10^5 pulses of 0.48 ms duration and of an intensity of L_{abs} = 0.55 GW/m² (F_{HF} = 12 MWs^{½}/m²) applied with a frequency of 25 Hz at a base temperature of T_{base} = 700 °C (homogeneous surface temperature). A second block of W1TiC material was available which was tested at a reduced power density of L_{abs} = 0.14 GW/m² (F_{HF} = 3 MWs^{½}/m²) (all other parameters were kept unaltered). This allowed comparing the materials among each other and to the reference tungsten IGP. Due to the PIM production process no preferential grain elongation exists [13], however IGP is sintered and forged (from two orthogonal directions) and possesses a needle-like grain structure. The ITER specifications demand that the "longitudinal orientation of the elongated grains shall not be parallel to the surface" [8] hence this study compares the PIM tungsten materials to the IGP in transversal elongation orientation (elongation of grains perpendicular to the heat loaded surface, IGPT) and to the recrystallized IGP material (after 1 h at 1600 °C, IGPR). The latter is motivated by the fact that PIM tungsten is free of internal stresses due to the production process, i.e. basically already recrystallized.

High heat flux loading was done with the electron beam facility JUDITH 2 [14,15] using established procedures [16,17]. The electron beam provides an intensity profile with approximately Gaussian shape and a full width at half maximum of ~5.7 mm. Hence the loaded area is circular and can be considered homogeneously loaded (max. heat load deviation from center ± 5%) within a radius of ~1 mm around the center only. This inhomogeneity is comparable to the situation of THLs in the strike point of the ITER divertor. The results were investigated by laser profilometry (KF3 sensor from OPM Messtechnik GmbH), scanning electron microscopy (SEM) and metallographic cross sectioning within the homogeneously loaded area of r = 1 mm. Cross sectioning was done by cutting the samples with a diamond cutting blade, then grinding with SiC paper and polishing with diamond suspension carefully towards the center of the loaded spot, finishing with an etching step which results in better visibility of cracks and grain structure/boundaries.

3. Results

The reference material IGPT showed a crack network with few primary cracks of 10–15 µm width connected by thinner (<9 µm) cracks. Tungsten melt droplets (diameter up to ~40 µm) were found on the rugged surface. The crack network on IGPR had a similar appearance, but the primary cracks were wider (up to 50 µm). The surface was less rugged and did not feature melt droplets (Fig. 5).

The sample of material W2TiC failed after the first few pulses and the experiment had to be stopped. Part of the surface flaked off (Fig. 1) and immediately overheated. The investigation of the cross section showed two features: first, a change in microstructure at a depth of

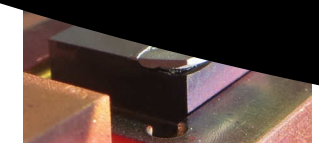

Fig. 1. Block of W2TiC material after delamination failure during the first few pulses of the test. The circular loaded area close to the center of the sample is visible next to the top surface crack.

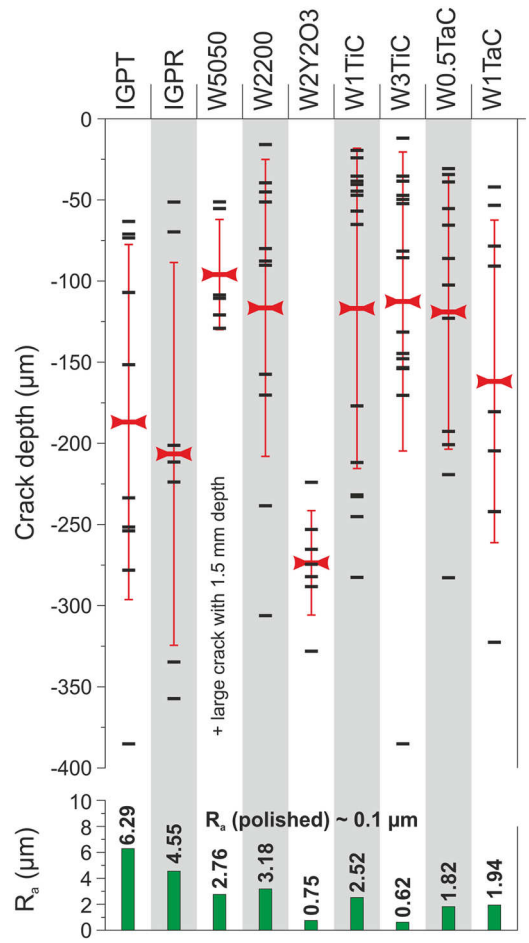

Fig. 2. The diagram shows the crack depth (top) and roughness R_a (bottom) measured for each material after 10^5 transient pulses of Δt = 0.48 ms and an intensity of L_{abs} = 0.55 GW/m² (F_{HF} = 12 MWs^{½}/m²) at T_{base} = 700 °C. Every horizontal black line in the crack depth diagram represents one crack and its depth, while the red indicators and their error bars show the average crack depths and their standard deviations, respectively. The exceptionally deep crack in the sample of material W5050 was excluded from the analysis.

100–200 µm. The grain size in the near surface area is larger, but the porosity lower. This is from a well-known grain growth process of near surface grains that can happen during production (sintering) [18]. Second, yellow inclusions were found in the delaminated part. An EDX analysis showed strong signals of Ti and N, suggesting the presence of TiN.

All other materials showed mostly intergranular crack networks with different degrees of roughening and crack depths (Fig. 2). The cracks grew perpendicular to the surface with little tortuosity of 1–1.3 (ratio of crack length to distance between the ends) and branching was rarely observed (Figs. 3 and 5).

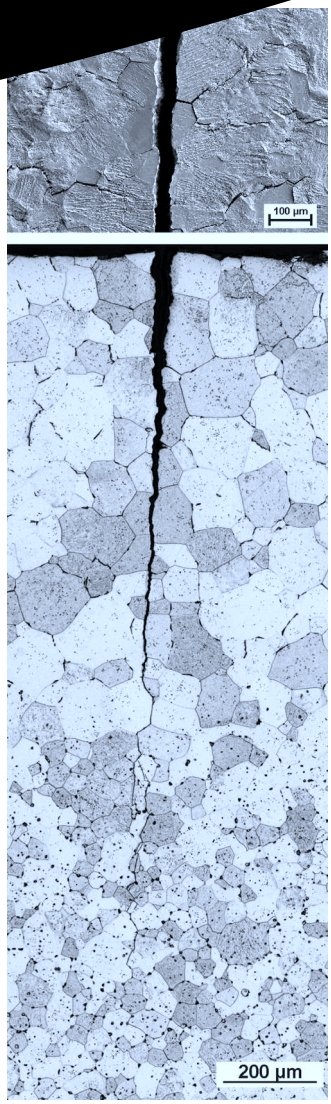

Fig. 3. SEM top view image (top) and light microscope image of the cross section (bottom) of the W5050 material sample. Both show the large and broad crack that formed and propagated transgranular through the near surface zone of larger grains. The bulk microstructure is visible at the bottom where the crack propagated intergranular.

Material W5050 had one particularly broad crack in its crack network (Fig. 3). The SEM image showed a width of ~50 µm, while all other cracks are similar in width (~15 µm or less, average ~6 µm). In the cross section it was found that this crack was 1.5 mm deep, while all other cracks are less than 130 µm deep. Additionally, roughening of the edges of the large crack is less pronounced. This strongly indicates an early formation of the large crack, probably due to material inhomogeneity, which led to stress relief and hence less growth of the other cracks. The cross section showed a change in microstructure at a depth of ~1 mm from the production process. In contrast to the previously described W2TiC, this change is not only deeper, but the difference in grain size and porosity is also much more pronounced (Fig. 3). The crack propagated transgranular in the zone of increased grain size and continued intergranular in the bulk.

Material W2Y2O3 showed very low roughening, but regular, deep cracks. The average crack depth is the highest of all tested materials and – in contrast to the other PIM materials – higher than the average crack depth of the reference materials (Fig. 2). The crack network showed primary cracks of typically 6–10 µm width and secondary cracks of <3 µm width. Melt droplets were found on the surface; however, an

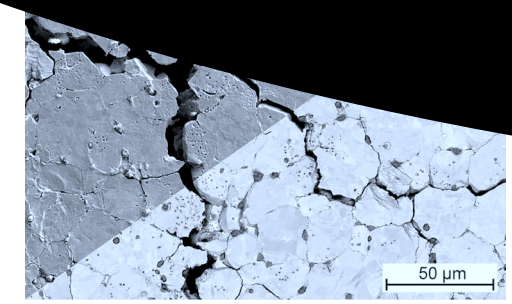

Fig. 4. SEM image composed of a secondary electron (SE) contrast image (upper left) and a backscattered electron (BSE) contrast image (lower right) of the surface of material W2Y2O3 after testing. Small melt droplets are clearly visible in the SE contrast, while their lower atomic number is revealed in the BSE contrast, indicating they consist of Y_2O_3. The image features examples for primary (wide, left) and secondary (thin, right) cracks.

EDX measurement proved that these were molten Y_2O_3 particles, not tungsten. Large droplets were mostly found at grain boundaries, smaller droplets appeared in holes in the grain area (Fig. 4).

The materials W2200, W1TiC, W3TiC, W0.5TaC, and W1TaC showed no peculiarities, just crack networks, with crack depths and roughness values lower than the reference materials (Figs. 2 and 5). However, the crack networks had slightly different characteristics: W2200 showed a primary crack network with broad cracks, typically 20–30 µm wide (maximum ~40 µm), and short thin secondary cracks of <3 µm width. On W1TiC a few short but wide cracks (~50 µm) were connected by cracks of up to 15 µm width forming a network with additional branches of thin cracks (<3 µm wide). The sample of W3TiC material had 3–4 larger cracks of ~15 µm width connected via a

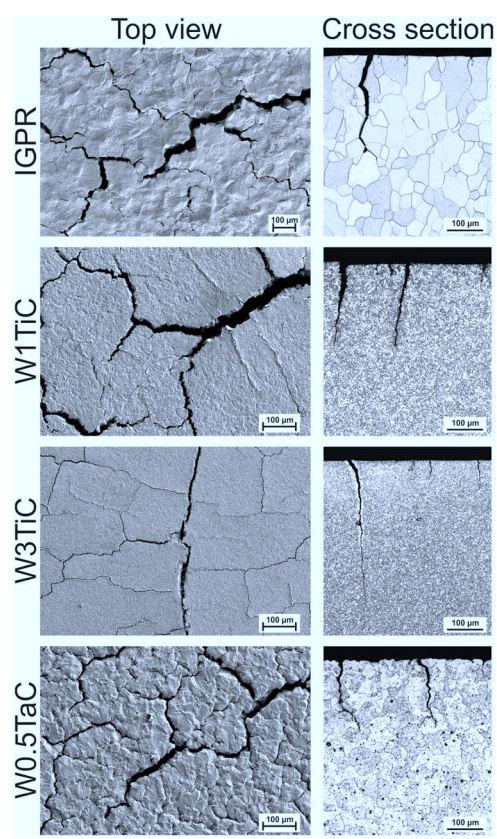

Fig. 5. SEM top view images (left) and light microscope images of the cross sections (right) of some of the material samples.

[illegible] of typically 2–3 μm (maximum [illegible] and W1TaC showed similar crack networks [illegible] (W0.5TaC) or mostly (W1TaC) larger cracks of [illegible] μm width connected by secondary branches of 2–5 μm width.

The second sample of material W1TiC which was subjected to a four times lower power density did not show cracks, just roughening of the surface (R_a = 0.22 μm). The reference material IGPT showed no damage under these conditions, while testing the reference material after recrystallization (IGPR) showed roughening only (R_a = 0.6 μm).

4. Discussion & conclusions

The experiments performed show a high pulse number damage behavior of some of the PIM tungsten materials that is generally comparable with IGPR. In particular W2200, W1TiC, W0.5TaC and W1TaC developed similar surface damages (crack networks/roughening), but outperform the reference with respect to crack depth and degree of roughening. The lower roughness values indicate a yield strength higher than that of IGPR can be expected for these materials. The lower crack depth would be explained by higher ultimate tensile strength and/or lower thermal conductivity [19].

Material W2TiC failed, probably due to inhomogeneities from production (TiN inclusions were found) that led to brittle crack propagation since the test was done on the materials W1TiC and W3TiC without failure. However, W3TiC also showed a particularly deep crack (Fig. 2). Tensile tests of the W1TiC material by C. Yin et al. show its ductile behavior at 600 °C [20]. In conclusion, since using TiC additions of more than 1 wt% yielded irregular results, either further optimization of the production process is necessary or additions of more than 1 wt% of TiC are detrimental for the thermal shock behavior.

While it is bold to draw conclusions for the different PIM materials it is clear that the results demonstrate the general ability of PIM materials to compete with or even outperform the reference materials with respect to high pulse number thermal shock performance. However, there is still room for optimization and since the PIM process allows the addition of a large variety of additives which can yield improvements in mechanical properties (and hence thermal shock performance), further tests on new material compositions produced by an optimized production route are planned.

Acknowledgments

This work has been carried out within the framework of the EUROfusion Consortium and has received funding from the Euratom research and training programme 2014-2018 under grant agreement [illegible] reflect th[illegible]

References

[1] Y. Koza, et al., J. Nucl. Mater. 329–333 (2004) 706–710, https:// [illegible] jnucmat.2004.04.187.
[2] G. Pintsuk, W. Kühnlein, J. Linke, M. Rödig, Fus. Eng. Des. 82 (2007) 1720–1729, https://doi.org/10.1016/j.fusengdes.2007.06.030.
[3] M. Wirtz, J. Linke, G. Pintsuk, L.A. Singheiser, I. Uytdenhouwen, Phys. Scr. T 145 (2011) 014058, , https://doi.org/10.1088/0031-8949/2011/T145/014058.
[4] Th. Loewenhoff, J. Linke, G. Pintsuk, C. Thomser, Fus. Eng. Des. 87 (2012) 1201–1205, https://doi.org/10.1016/j.fusengdes.2012.02.106.
[5] R.A. Pitts, S. Carpentier, F. Escourbiac, T. Hirai, V. Komarov, S. Lisgo, A.S. Kukushkin, A. Loarte, M. Merola, A.S. Naik, R. Mitteau, M. Sugihara, B. Bazylev, P.C. Stangeby, J. Nucl. Mater. 438 (2013) (2013) S48–S56, https://doi.org/10.1016/j.jnucmat.2013.01.008.
[6] M. Wirtz, J. Linke, Th. Loewenhoff, G. Pintsuk, I. Uytdenhouwen, Phys. Scr. T 167 (2016) 014015, , https://doi.org/10.1088/0031-8949/T167/1/014015.
[7] M. Wirtz, I. Uytdenhouwen, V. Barabash, F. Escourbiac, T. Hirai, J. Linke, Th. Loewenhoff, S. Panayotis, G. Pintsuk, Nucl. Fus. 57 (2017) 066018, , https://doi.org/10.1088/1741-4326/aa6938.
[8] V. Barabash, "Material specification for the supply of tungsten plates for the ITER divertor", ITER_D_2EDZJ4 v1.3 (10.03.2009).
[9] T. Hirai, et al., Nucl. Mater. Energy 9 (2016) 616–622, https://doi.org/10.1016/j.nme.2016.07.003.
[10] G. Pintsuk, et al., Phys. Scr. T 167 (2016) 014056, , https://doi.org/10.1088/0031-8949/T167/1/014056.
[11] S. Antusch, L. Commin, M. Müller, V. Piotter, T. Weingaertner, J. Nucl. Mater. 447 (2014) 314–317, https://doi.org/10.1016/j.jnucmat.2013.11.007.
[12] S. Antusch, D.E.J. Armstrong, T.B. Britton, L. Commin, J.S.K.-L. Gibson, H. Greuner, J. Hoffmann, W. Knabl, G. Pintsuk, M. Rieth, S.G. Roberts, T. Weingaertner, Nucl. Mater. Energy 3-4 (2015) 22–31, https://doi.org/10.1016/j.nme.2015.04.002.
[13] S. Antusch, J. Reiser, J. Hoffmann, A. Onea, Refractory materials for energy applications, Energy Technol. 5 (2017) 1064–1070, https://doi.org/10.1002/ente.201600571.
[14] P. Majerus, et al., ; The new electron beam test facility JUDITH II for high heat flux experiments on plasma facing components, Fus. Eng. Des. 75–79 (365–369) (2005), https://doi.org/10.1016/j.fusengdes.2005.06.058.
[15] A. Schmidt, et al., High Heat Flux Testing of components for future fusion devices by means of the facility JUDITH 2, International Conference on High-Power Electron Beam Technology 2010 (EBEAM 2010), 1 Curran Associates, Inc., 2011, p. 571.
[16] Th. Loewenhoff, T. Hirai, S. Keusemann, J. Linke, G. Pintsuk, A. Schmidt, J. Nucl. Mater. 415 (2011) S51–S54, https://doi.org/10.1016/j.jnucmat.2010.08.065.
[17] Th. Loewenhoff, Combined Steady State and High Cycle Transient Heat Load Simulation with the Electron Beam Facility JUDITH 2, PhD thesis RWTH Aachen, 2012.
[18] S. Antusch, E. Visca, A. Klein, H. Walter, K. Pursche, M. Wirtz, Th. Loewenhoff, H. Greuner, B. Böswirth, J. Hoffmann, D. Bolich, G. Pintsuk, M. Rieth; Manufacturing, high heat flux testing and post mortem analyses of a W-PIM mock-up, 2019 (submitted).
[19] M. Wirtz, Thermal Shock Behaviour of Different Tungsten Grades Under Varying Preconditions, PhD thesis RWTH Aachen, 2012.
[20] C. Yin, et al., Int. J. Refract. Met. Hard Materials 75 (2018) 153–162, https://doi.org/10.1016/j.ijrmhm.2018.04.003.